Journal of Catalysis 443 (2025) 115970

Contents lists available at ScienceDirect

Journal of Catalysis

journal homepage: www.elsevier.com/locate/jcat

Research article

Degree of span control to determine the impact of different mechanisms and limiting steps: Oxygen evolution reaction over $Co_3O_4(001)$ as a case study

Kapil Dhaka [a], Kai S. Exner [a,b,c,*]

[a] University of Duisburg-Essen, Faculty of Chemistry, Theoretical Catalysis and Electrochemistry, Universitätsstraße 5, 45141 Essen, Germany
[b] Cluster of Excellence RESOLV, 44801 Bochum, Germany
[c] Center for Nanointegration (CENIDE) Duisburg-Essen, 47057 Duisburg, Germany

ARTICLE INFO

Keywords:
Oxygen evolution reaction
Co_3O_4
Descriptor approach
Reaction mechanism
Degree of rate control

ABSTRACT

Oxygen evolution reaction (OER) is the limiting process in electrolyzers for the production of green hydrogen. Although computational studies using density functional theory calculations provide insights into reaction mechanisms and limiting steps of OER catalysts, our mechanistic understanding is still limited even for state-of-the-art OER catalysts. This finding can be related to the fact that most computational studies rely on the approximation of the electrocatalytic activity by a single reaction mechanism and the limiting reaction step is solved by thermodynamic considerations, thereby assuming that the reaction rate is determined by a single step only. In this article, we present a framework to account for the mechanistic diversity in the formation of gaseous oxygen, using the example of a Co_3O_4 model catalyst due to the use of cobalt oxide-based materials in alkaline electrolysis. In addition to traditional reaction mechanisms, we consider Walden-like pathways in the analysis and show that multiple reaction mechanisms compete under OER conditions. To gain unprecedented insight into the limiting reaction steps, we introduce the concept of degree of span control, a thermodynamic representation based on Campbell's generalized degree of rate control from thermal catalysis but aimed at the study of electrocatalytic processes. We demonstrate that in the OER over $Co_3O_4(001)$, different reaction steps contribute to the OER current density to a different extent when the applied electrode potential is modulated. The degree of span control framework is considered useful for screening reaction mechanisms and limiting steps of catalytic processes at electrified solid–liquid interfaces before performing kinetic studies of selected elementary steps.

1. Introduction

Oxygen evolution reaction (OER) – $2H_2O \rightarrow O_2 + 4H^+ + 4e^-$, $U^0_{OER} = 1.23$ V *vs.* reversible hydrogen electrode (RHE) – represents the bottleneck in proton exchange membrane (PEM) electrolyzers for the production of gaseous hydrogen as energy carrier [1]. Even for solar cell applications operating at moderate current densities of about 10 mA/cm^2, [2] today's OER catalysts require an overpotential on the order of several hundred mV, [3] which poses a significant challenge for efficient and sustainable hydrogen production by water electrolysis [4].

In recent decades, electronic structure calculations in the density functional theory approximation have guided the development of advanced materials for electrocatalytic processes including the OER [5–8]. There is consensus that identifying limiting reaction steps could lead to the development of electrocatalysts with improved catalytic properties by alleviating the kinetic bottleneck in the reaction mechanism [9]. While Campbell introduced a powerful concept for the discussion of the kinetics in thermal catalysis by referring to the generalized degree of rate control, [10–13] on the contrary, in electrocatalysis it is still common to analyze reaction mechanisms through thermodynamic considerations [14]. The main reason for this fact is that the calculation of transition states at constant potential is computationally demanding and thus limits the applicability of kinetic considerations for complex catalytic processes with several proton-coupled electron transfer steps in the reaction mechanism [15–18]. On the other hand, Nørskov and coworkers developed a framework to render activity predictions by analyzing the thermodynamic part of the free-energy landscape, which is based on extracting the largest free-energy change

* Corresponding author.
E-mail address: kai.exner@uni-due.de (K.S. Exner).

https://doi.org/10.1016/j.jcat.2025.115970
Received 28 December 2024; Accepted 31 December 2024
Available online 22 January 2025

at the equilibrium potential of the electrocatalytic process [19]. The corresponding activity descriptor is coined the thermodynamic overpotential, η_{TD}, which has gained unprecedented popularity in the electrochemistry community due to its simplicity [20].

Despite the success in identifying material motifs for electrocatalytic processes using the concept of η_{TD}, [21] there are several limitations in applying this type of analysis. First, the descriptor η_{TD} refers to the so-called potential-determining step (PDS) and therefore does not necessarily correspond to the rate-determining step (RDS) that controls the kinetics [22,23]. Secondly, the adoption of a single PDS or RDS is another assumption that is not necessarily met for complex proton-coupled electron transfer steps in electrocatalysis; rather, it is also possible that several steps contribute to the reaction rate (current density) to varying degrees [24]. This fact has so far been largely overlooked in the analysis of free-energy landscapes for electrocatalytic transformations including the OER where cobalt oxide has emerged as a state-of-the-art material for alkaline electrolysis due to its catalytic properties and stability under the harsh anodic conditions [25].

Previous theoretical works analyzed the OER over different phases of Co-based oxides and identified limiting reaction steps in the approximation of the descriptor η_{TD} [26–29]. Most of these studies relied on a single mechanistic description by referring to the mononuclear mechanism, [30] thus leaving a gap in the mechanistic understanding of the OER on Co_3O_4. Given that Co_3O_4 belongs to the most active catalysts in the alkaline OER, a recent data-driven study suggested that several reaction mechanisms rather than a single pathway lead to the formation of gaseous O_2 [31]. This statement is further supported by the work of Amin and Baltruschat, [32] who highlighted the need to comprehend the detailed elementary steps of the OER over Co_3O_4 as this could help improve the catalyst performance. Their study demonstrates that only the surface atoms of the Co_3O_4 spinel catalyst participate in the OER, as demonstrated by ^{18}O isotope labeling and DEMS measurements, while a fraction of about 12–34 % of the surface atoms are catalytically active. To this end, mechanistic pathways containing lattice oxygen, often referred to as lattice oxygen evolution mechanisms, can be fairly excluded in the analysis [33–36].

In the present manuscript, we overcome the above-mentioned shortcomings by presenting two major extensions: a) For a $Co_3O_4(001)$ surface as a model system for cobalt oxides, we study the elementary steps of the OER by considering a variety of different pathways in the analysis of free-energy diagrams. In addition to conventional reaction mechanisms, our mechanistic models also consider Walden-type pathways consisting of concerted adsorption–desorption steps. Only recently, it has been reported that these mechanisms are relevant for the elementary steps in the oxygen electrocatalysis [37–39]. b) Based on the free-energy diagrams for the different reaction mechanisms in the OER over $Co_3O_4(001)$, we introduce the potential-dependent degree of span control as a new concept to assess the contribution of each mechanism or reaction step to the reaction rate (current density). This allows us to unravel the potential-dependent mechanistic complexity of the OER over a model material, since multiple mechanisms and elementary steps may contribute to the reaction rate to a different extent when the applied overpotential is varied. Implementing these extensions in future work may facilitate systematic and unbiased exploration of reaction networks for electrocatalytic reactions even beyond the OER, which in turn can advance the discovery of catalytic materials using data science techniques, including artificial intelligence.

2. Theoretical model

We apply electronic structure calculations in the density functional theory framework including a Hubbard U correction, using the Vienna Ab initio Simulation Package (VASP) with the VASPsol extension [40–43]. All computational details are summarized in section S1 of the supporting information (SI). There, we also discuss the magnetic moments of Co and our surface model for studying $Co_3O_4(001)$, the details of which are given in section S2. The modeling of electrochemical reaction steps using the computational hydrogen electrode (CHE) approach is described in section S3. A benchmarking of our computational approach including the choice of the Hubbard U value is provided in section S7 of the SI.

The OER is a complex process that requires the transfer of four proton-electron pairs to produce a single oxygen molecule. To gain insight into the elementary steps under the harsh anodic reaction conditions ($U > 1.23$ V *vs.* RHE), we incorporate a variety of different reaction mechanisms [44] into the analysis of free-energy diagrams along the reaction coordinate. The reaction equations for the elementary steps of each pathway are listed below.

2.1. Traditional OER mechanisms

2.1.1. Mononuclear mechanism

In previous computational studies on the OER, the most extensively employed mechanism refers to the mononuclear description, which consists of the subsequent formation of the *OH, *O, and *OOH intermediates: [30,45].

$$* + H_2O_{(l)} \rightarrow *OH + (H^+ + e^-),\ \Delta G_1 \quad (1)$$

$$*OH \rightarrow *O + (H^+ + e^-),\ \Delta G_2 \quad (2)$$

$$*O + H_2O_{(l)} \rightarrow *OOH + (H^+ + e^-),\ \Delta G_3 \quad (3)$$

$$*OOH \rightarrow * + (H^+ + e^-) + O_{2(g)},\ \Delta G_4 \quad (4)$$

note that * indicates an active surface site of the electrocatalyst, such as a surface Co atom in the case of $Co_3O_4(001)$.

2.1.2. Bifunctional I mechanism

While the mononuclear mechanism refers to the category of a single-site mechanism, other OER pathways require two adjacent sites to catalyze the formation of gaseous oxygen. In case of bifunctional pathways, the second site is reconciled with surface oxygen, $*O_A$, which can act as a Brønsted base by accepting a proton and an electron from the reactant water. The main difference of the bifunctional I mechanism from the mononuclear description is that the formation of the *OOH intermediate is bypassed, and an *OO adsorbate is formed instead [46].

$$* + *O_A + H_2O_{(l)} \rightarrow *OH + *O_A + (H^+ + e^-),\ \Delta G_5 \quad (5)$$

$$*OH + *O_A \rightarrow *O + *O_A + (H^+ + e^-),\ \Delta G_6 \quad (6)$$

$$*O + *O_A + H_2O_{(l)} \rightarrow *OO + *OH_A + (H^+ + e^-),\ \Delta G_7 \quad (7)$$

$$*OO + *OH_A \rightarrow * + *O_A + (H^+ + e^-) + O_{2(g)},\ \Delta G_8 \quad (8)$$

2.1.3. Bifunctional II mechanism

While the bifunctional II mechanism [47–49] also includes a second site, $*O_A$, in the mechanistic description, the difference to the bifunctional I mechanism is the occurrence of a chemical reaction step: the second water molecule is adsorbed onto the surface without the direct release of a proton-electron pair (*cf.* Eq. (11)). Therefore, this pathway consists of five elementary steps in total.

$$* + *O_A + H_2O_{(l)} \rightarrow *OH + *O_A + (H^+ + e^-),\ \Delta G_9 \quad (9)$$

$$*OH + *O_A \rightarrow *O + *O_A + (H^+ + e^-),\ \Delta G_{10} \quad (10)$$

$$*O + *O_A + H_2O_{(l)} \rightarrow *OOH + *OH_A,\ \Delta G_{11} \quad (11)$$

$$*OOH + *OH_A \rightarrow *OOH + *O_A + (H^+ + e^-),\ \Delta G_{12} \quad (12)$$

$$*OOH + *O_A \rightarrow * + *O_A + (H^+ + e^-) + O_{2(g)},\ \Delta G_{13} \quad (13)$$

2.1.4. Binuclear mechanism

In the binuclear mechanism [50,51], two adjacent metal sites are needed to facilitate the production of gaseous O_2 through the recombination of two adjacent oxygen adsorbates (*cf.* Eq. (18)). The last reaction step is, similar to the splitting of the second water molecule in the bifunctional II mechanism (*cf.* Eq. (11)), a chemical reaction step so that the entire mechanistic description contains five elementary steps.

$$* + * + H_2O_{(l)} \rightarrow *OH + * + (H^+ + e^-),\ \Delta G_{14} \quad (14)$$

$$*OH + * + H_2O_{(l)} \rightarrow *OH + *OH + (H^+ + e^-),\ \Delta G_{15} \quad (15)$$

$$*OH + *OH \rightarrow *O + *OH + (H^+ + e^-),\ \Delta G_{16} \quad (16)$$

$$*O + *OH \rightarrow *O + *O + (H^+ + e^-),\ \Delta G_{17} \quad (17)$$

$$*O + *O \rightarrow * + * + O_{2(g)},\ \Delta G_{18} \quad (18)$$

2.1.5. Oxide mechanism

Like the binuclear mechanism, the oxide mechanism [52,53] requires two adjacent metal sites for the formation of gaseous O_2. The starting point of this mechanism is different because the surface needs to be completely covered with oxygen (*O + *O). After the formation of two adjacent *OO intermediates, the outermost oxygen atoms of the *OO adsorbates recombine to form O_2 in a chemical reaction step (*cf.* Eq. (23)).

$$*O + *O + H_2O_{(l)} \rightarrow *OOH + *O + (H^+ + e^-),\ \Delta G_{19} \quad (19)$$

$$*OOH + *O + H_2O_{(l)} \rightarrow *OOH + *OOH + (H^+ + e^-),\ \Delta G_{20} \quad (20)$$

$$*OOH + *OOH \rightarrow *OOH + *OO + (H^+ + e^-),\ \Delta G_{21} \quad (21)$$

$$*OOH + *OO \rightarrow *OO + *OO + (H^+ + e^-),\ \Delta G_{22} \quad (22)$$

$$*OO + *OO \rightarrow *O + *O + O_{2(g)},\ \Delta G_{23} \quad (23)$$

2.2. Walden-type mechanisms

All the previously discussed reaction mechanisms are based on the notion that the unoccupied metal site, *, is restored after the product O_2 is formed. However, it is also conceivable that product desorption and reactant adsorption occur simultaneously, and the corresponding mechanisms are coined Walden pathways [38,39,54]. The peculiarity of the Walden mechanisms is that the unoccupied metal center is no longer part of the reaction mechanism, since the active center is covered by an adsorbate in all steps of the catalytic cycle.

We emphasize that it is possible to derive Walden-type mechanisms for all the above pathways. However, we note that we have omitted the oxide-Walden and binuclear-Walden pathways from our investigations as these pathways already necessitate the presence of two adjacent metal sites in the reaction mechanism. A Walden inversion step is considered unlikely in such a situation due to steric hindrances, since in addition to the oxygen molecule, two water molecules are involved in a single elementary step. To this end, we restrict the analysis of Walden-type pathways to mechanisms requiring a single metal site or a single metal site and a neighboring acceptor site not being involved in the Walden step, which is met for the case of the mononuclear and bifunctional descriptions, respectively. The corresponding reaction equations for the elementary steps of the mononuclear-Walden and bifunctional-Walden pathways are given in the below.

2.2.1. Mononuclear-Walden mechanism

The mononuclear-Walden description is reminiscent of the mechanistic description of Eqs. (1)–(4). Instead of producing gaseous O_2 directly from the *OOH intermediate, the *OO adsorbate is formed (*cf.* Eq. (26)), which undergoes a Walden-like step with the reactant water (*cf.* Eq. (27)).

$$*OH \rightarrow *O + (H^+ + e^-),\ \Delta G_{24} \quad (24)$$

$$*O + H_2O_{(l)} \rightarrow *OOH + (H^+ + e^-),\ \Delta G_{25} \quad (25)$$

$$*OOH \rightarrow *OO + (H^+ + e^-),\ \Delta G_{26} \quad (26)$$

$$*OO + H_2O_{(l)} \rightarrow *OH + (H^+ + e^-) + O_{2(g)},\ \Delta G_{27} \quad (27)$$

2.2.2. Bifunctional-Walden mechanism

The bifunctional-Walden mechanism is based on the bifunctional I description (*cf.* Eqs. (5)–(8)). The Walden-like step is given by Eq. (31), which is identical to the mononuclear-Walden description (*cf.* Eq. (27)).

$$*OH + *O_A \rightarrow *O + *O_A + (H^+ + e^-),\ \Delta G_{28} \quad (28)$$

$$*O + *O_A + H_2O_{(l)} \rightarrow *OO + *OH_A + (H^+ + e^-),\ \Delta G_{29} \quad (29)$$

$$*OO + *OH_A \rightarrow *OO + *O_A + (H^+ + e^-),\ \Delta G_{30} \quad (30)$$

$$*OO + *O_A + H_2O_{(l)} \rightarrow *OH + *O_A + (H^+ + e^-) + O_{2(g)},\ \Delta G_{31} \quad (31)$$

Fig. 1 provides an overview of the seven mechanistic descriptions in question for the OER over Co_3O_4(001).

2.3. Analysis of free-energy diagrams: Activity descriptor $G_{max}(U)$

We construct potential-dependent free-energy diagrams using the CHE approach [19] for the mechanistic descriptions summarized in Fig. 1. These free-energy landscapes are analyzed by the descriptor $G_{\max}(U)$, [55] which is a representation of the free-energy span model [56] for catalytic processes at electrified solid/ liquid interfaces, to estimate the electrocatalytic activity. As outlined in the introduction section, the most popular activity descriptor in the OER refers to the thermodynamic overpotential, η_{TD}, which extracts the largest free-energy change of a given mechanistic description at the OER equilibrium potential [55]. In the following, we discuss the differences of η_{TD} and $G_{\max}(U)$ using the example of the mononuclear mechanism (*cf.* Eqs. (1)–(4)):

$$\eta_{TD} = (\max\{\Delta G_1, \Delta G_2, \Delta G_3, \Delta G_4\} - 1.23\ \text{eV})/e \quad (32)$$

As evident from Eq. (32), the descriptor η_{TD} predicts activity trends in the OER under equilibrium conditions by relying on the notion that a single elementary step governs the reaction rate, without taking the applied overpotential or the kinetics into account. The descriptor $G_{\max}(U)$ aims to overcome the shortcomings of the η_{TD} approach: instead of relying on the tacit assumption that a single elementary step is limiting the reaction rate, it is considered that several elementary steps can contribute to the reaction rate by assessing the reaction rate through the concept of a span model [57]. In addition, it is taken into account that the limiting span can change if the applied overpotential is modulated. In case of the mononuclear mechanism (*cf.* Eqs. (1)–(4)), the free energies of the intermediate states in the OER cycle are:

$$G(*) = 0\ \text{eV} \quad (33)$$

$$G(*OH) = \Delta G_1 - 1 \cdot e \cdot U \quad (34)$$

$$G(*O) = \Delta G_1 + \Delta G_2 - 2 \cdot e \cdot U \quad (35)$$

$$G(*OOH) = \Delta G_1 + \Delta G_2 + \Delta G_3 - 3 \cdot e \cdot U \quad (36)$$

$$G(* + O_2) = \Delta G_1 + \Delta G_2 + \Delta G_3 + \Delta G_4 - 4 \cdot e \cdot U = 4.92\ \text{eV} - 4 \cdot e \cdot U \quad (37)$$

Based on the free energies of Eqs. (33)–(37), the potential-dependent activity descriptor $G_{\max}(U)$ can be estimated at any applied electrode potential $U > 1.23$ V *vs.* RHE:

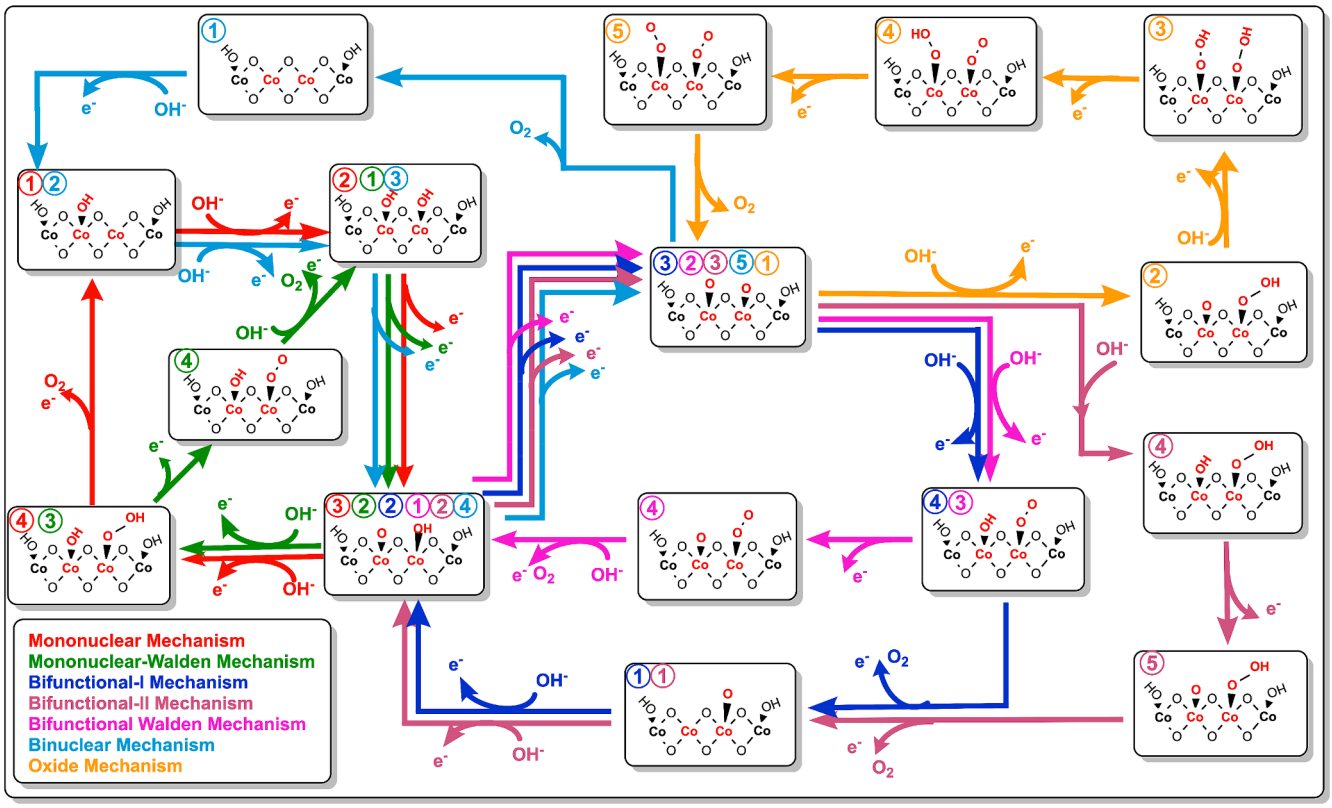

Fig. 1. Schematic representation of seven different mechanisms for the oxygen evolution reaction (OER) over Co_3O_4(001). The elementary steps of all pathways are listed in Eqs. (1)–(31).

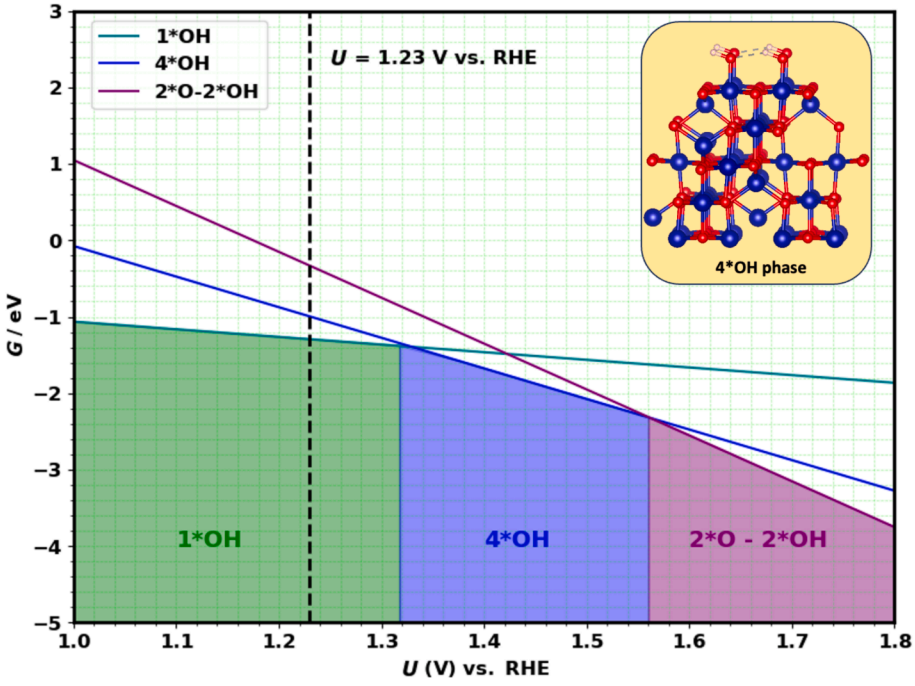

Fig. 2. Stability diagram of different surface configurations containing *OH and *O adsorbates on a Co_3O_4(001) surface under anodic conditions. Shaded regions indicate different stable surface phases: 1 *OH (green), 4 *OH (blue), and 2 *O − 2 *OH (purple). The vertical dashed line at $U = 1.23$ V *vs.* RHE indicates the equilibrium potential of the oxygen evolution reaction. An extended version of the stability diagram including all considered configurations can be found in **Fig. S2** (*cf.* section S3 of the SI). Inset: structure of the 4 *OH phase, which is thermodynamically stable under OER conditions. (For interpretation of the references to colour in this figure legend, the reader is referred to the web version of this article.)

$$G_{max}(U) = \max\{G(*OH) - G(*); G(*O) - G(*); G(*OOH) - G(*); G(*O) - G(*OH); G(*OOH) - G(*OH); G(* + O_2) - G(*OH); G(*OOH) - G(*O); G(* + O_2) - G(*O); G(* + O_2) - G(*OOH)\} \quad (38)$$

We use of the above concept to analyze free-energy diagrams for the various OER pathways (*cf.* Fig. 1) in section 3 of the main text. For an overview of the span model of the other OER mechanisms, we refer to section S5 of the SI or to the recent literature [58].

In analyzing the multiple OER mechanism, we present an extension of the $G_{max}(U)$ approach by deriving a framework titled "potential-dependent degree of span control". This concept, inspired by Campbell's work in thermal catalysis [10–13] and discussed further in the following section, allows us to unravel the contribution of each mechanistic pathway and each elementary step to the OER rate.

3. Results & discussion

3.1. Surface structure of $Co_3O_4(001)$ under OER conditions

To gain insight into the surface structure of a model $Co_3O_4(001)$ electrode under OER conditions, we apply the concept of surface Pourbaix diagrams [59–61]. In this approach, the thermodynamically most stable surface configuration is determined as a function of the environmental parameters; that is, the applied electrode potential U *vs.* RHE and pH. Further information on the application of the Pourbaix approach is provided in section S3 of the SI (*cf.* **Fig. S1**).

Fig. 2 shows a simplified representation of the Pourbaix approach for $Co_3O_4(001)$ at applied electrode potentials above 1 V *vs.* RHE. We observe that three different phases turn out to be stable in dependence of the applied electrode potential: a) 1 *OH phase for 1.00 V < U *vs.* RHE < 1.32 V; b) 4 *OH phase for 1.32 V < U *vs.* RHE < 1.56 V; c) 2 *OH + 2 *O phase for 1.56 V < U *vs.* RHE < 1.80 V. We note that our stability diagram is in reasonable agreement with former theoretical investigations by Pentcheva and coworkers [26,62]. The slight difference in the observed potential windows for the thermodynamically stable phases can be ascribed to the consideration or neglection of the aqueous environment in the DFT calculations [63].

While the stability diagram of Fig. 2 reveals that the $Co_3O_4(001)$ is only partially covered by *OH adsorbates (coverage of 25 %) at the equilibrium potential of the OER, a complete *OH coverage becomes energetically favored for applied electrode potentials above 1.32 V *vs.* RHE. Considering that Co_3O_4-based materials require an applied overpotential of at least 300 mV to reach a current density on the order of 10 mA/cm^2 in the OER, [64] we use the 4 *OH phase (*cf.* inset of Fig. 2), also denoted as $Co_3O_4(001)$-4*OH, for our mechanistic studies based on the introduced reaction pathways (*cf.* Fig. 1).

3.2. Mechanistic analysis of the OER over $Co_3O_4(001)$-4*OH

We determine the free-energy changes for the elementary reaction steps of Eqs. (1)–(31) (*cf.* section 2) and construct free-energy diagrams along the reaction coordinate for the considered reaction mechanisms. All calculated free-energy changes are tabulated in section S4 of the SI (*cf.* **Table S1**). Fig. 3 depicts the free-energy diagrams for the seven mechanistic pathways at an applied electrode potential of $U = 1.53$ V *vs.* RHE, on the basis of which the activity descriptor $G_{max}(U = 1.53\ V)$ is determined. Section S5 of the SI provides an overview of how this descriptor is derived by extracting the largest free-energy span among the free energies of the reaction intermediates (*cf.* **Table S1**). Potential-dependent values for the descriptor $G_{max}(U)$ at $U = 1.23$ V, 1.33 V, and 1.53 V *vs.* RHE are given in Table 1.

Fig. 3 indicates that there are three mechanistic descriptions with a similar value of $G_{max}(U = 1.53\ V)$: while the mononuclear and bifunctional-Walden mechanisms reveal $G_{max}(U = 1.53\ V) = 0.08$ eV, we obtain $G_{max}(U = 1.53\ V) = 0.09$ eV for the mononuclear-Walden pathway. This finding already illustrates that several mechanisms compete for the formation of gaseous O_2 on $Co_3O_4(001)$, and the picture of a single mechanistic description, as used in previous theoretical studies, is not sufficient for thorough contemplation of the limiting reaction steps. Besides these three mechanisms, it has to be noted that the oxide and bifunctional II descriptions could also contribute to the OER rate due to slightly larger $G_{max}(U = 1.53\ V)$ values of 0.20 eV and 0.22

Table 1
$G_{max}(U)$ values as a measure for the electrocatalytic activity at three different applied electrode potentials ($U = 1.23$ V, 1.33 V, 1.53 V) *vs.* RHE for different OER mechanisms on the $Co_3O_4(001)$-4*OH surface.

	$G_{max}(U)$ / eV at U = (1.23 V, 1.33 V, 1.53 V) *vs.* RHE					
	Traditional pathways			Walden-type pathways		
	U = 1.23 V	U = 1.33 V	U = 1.53 V	U = 1.23 V	U = 1.33 V	U = 1.53 V
Mononuclear	0.41	0.28	0.08	0.39	0.29	0.09
Bifunctional-I	0.66	0.56	0.36	0.68	0.48	0.08
Bifunctional-II	0.50	0.40	0.22	–	–	–
Binuclear	0.68	0.52	0.52	–	–	–
Oxide	0.50	0.40	0.20	–	–	–

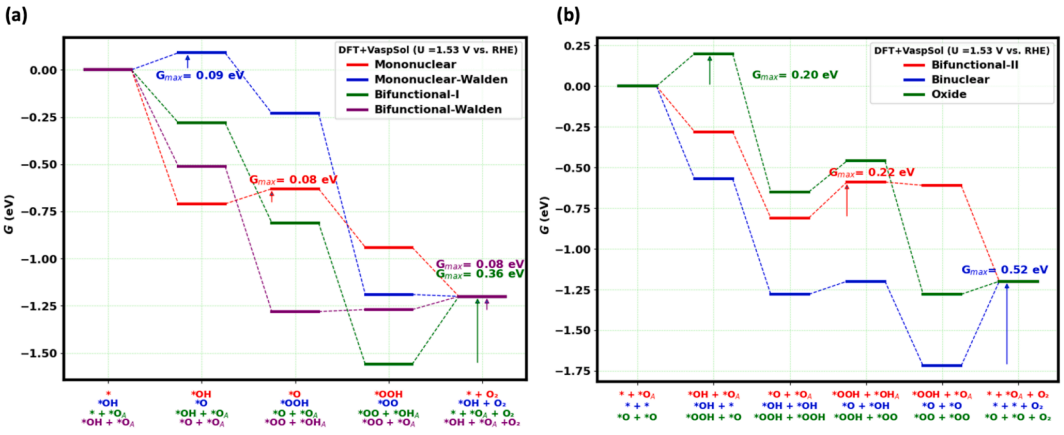

Fig. 3. Free-energy diagram for seven mechanistic descriptions of the oxygen evolution reaction (OER) on $Co_3O_4(001)$-4*OH at $U = 1.53$ V *vs.* RHE. For each OER pathway, the descriptor $G_{max}(U)$ is a measure for the electrocatalytic activity. Detailed potential-dependent free-energy diagrams for all pathways are provided in **Figs. S3-S9** (*cf.* section S6 of the SI).

eV, respectively. This statement is based on the fact that the descriptor $G_{max}(U = 1.53\ V)$ has a sensitivity of 0.20 eV and only if two mechanisms differ by more than 0.20 eV, the energetically unfavorable pathway can be excluded from the analysis [55]. For this reason, the bifunctional I and binuclear descriptions can be largely ignored for the mechanistic analysis of the OER on Co_3O_4(001).

Table 1 illustrates the potential dependence of the descriptor $G_{max}(U)$, which can also be recognized by potential-dependent free-energy diagrams (*cf.* **Figs. S3-S9** in section S6 of the SI). While the bifunctional-Walden mechanism belongs to the most active pathways at $U = 1.53$ V *vs.* RHE, a different situation is encountered at $U = 1.23$ V *vs.* RHE, where this mechanism is not favored compared to the mononuclear description (the difference in $G_{max}(U)$ exceeds 0.20 eV). This finding highlights that the applied electrode potential can modulate the influence of different mechanistic descriptions in the OER, making it necessary to elucidate the contribution of each pathway depending on the driving force for the electrocatalytic process. This is achieved by the introduction of the potential-dependent degree of span control as described below.

3.3. The potential-dependent degree of span control

In the field of electrocatalysis, it is a widely accepted notion that the overall reaction rate is determined by a single elementary step, which is referred to as the rate-determining step (RDS) [65]. The RDS is commonly approximated by means of the potential-determining step (PDS) when DFT calculations are used to identify the limiting step in the mechanistic cycle [66]. This conceptualization simplifies the complex nature of electrocatalytic processes, although multiple steps can collectively influence the rate. One reason for this simplification can be found in the discussion of the Tafel slope in experimental investigations: a linear Tafel regime is often interpreted in such a way that a single RDS determines the kinetic description, and a change in the Tafel slope is attributed to a switch in the RDS. However, a recent study by Koper and coworkers has outlined that a switch in the Tafel slope can also be related to factors beyond the traditional view [67]. In addition to mass transport or the influence of the catalyst layer, a change in the Tafel slope can also be related to a change in the surface coverage due to the shift of the pre-equilibrium for steps before the RDS at different electrode potentials [68]. We note that a shift of the pre-equilibrium is also embedded in the descriptor $G_{max}(U)$ (*cf.* section 2.3), since with increasing overpotential the number of steps determining $G_{max}(U)$ is reduced (*cf.* **Figs. S3-S9** in section S6 of the SI).

In a recent communication by Exner applying the concept of the generalized degree of rate control, it was reported that even in a linear Tafel regime, multiple steps can contribute to the reaction rate [24]. The contribution of the elementary reaction steps that are not reconciled with the RDS can be as high as 25 %, which does not seem negligible if one wants to gain unprecedented insights into the nature of the limiting reaction steps. To this end, there is a need to derive a framework that allows determining the contribution of different reaction mechanisms and reaction steps to the current density of an electrocatalytic process. While it would be straightforward to transfer Campbell's generalized degree of rate control [10–12] from thermal catalysis to electrocatalysis (as already reported in some studies using microkinetic models [24,69,70]), the main caveat of this line of thought relates to the complexity of determining transition states by DFT calculations for catalytic processes at electrified solid/liquid interfaces. Since the calculation of transition states for charge transfer steps is computationally intensive and time-consuming, [71] this strategy is not recommended for heuristic materials screening [72–74], which is widely used in the literature. Therefore, we introduce an approach that allows capturing the contribution of different reaction mechanisms and reaction steps to the current density in dependence of the applied electrode potential while still relying on the level of thermodynamics. This is achieved by applying the descriptor $G_{max}(U)$ in conjunction with a microkinetic model [55,58].

Our microkinetic model relies on the quasi-equilibrium assumption, which is a common approximation to investigate the kinetics of electrocatalytic processes [75]. The difference between the quasi-equilibrium and steady-state assumption has been discussed in a recent communication by one of the authors, [76] indicating that the quasi-equilibrium method approaches the steady-state assumption if there is no change in the active surface configuration. This restriction is fairly met for the case of Co_3O_4(001), since the 4 *OH phase is dominant under OER conditions (see Fig. 2). For all possible reaction mechanisms k, we calculate partial current densities, $j_k(U)$, as a function of the applied electrode potential according to Eq. (32). Note that this expression is valid in the Tafel regime of the current–potential relationship, that is, for overpotentials exceeding 30 mV: [77,78]

$$j_k(U) \propto \theta_k \bullet \mathrm{Exp}\left(\frac{-G_{max,k}(U)}{k_B \bullet T}\right) \tag{39}$$

The index k in Eq. (32) indicates the different mechanistic descriptions of the OER over Co_3O_4(001)-4*OH (*cf.* Fig. 1). Please note that the coverage term, θ_k, amounts to one for all reaction mechanisms due to the thermodynamic stability of the 4 *OH phase under OER conditions (*cf.* inset of Fig. 2). In addition, we emphasize that Eq. (32) is based on the adoption of a potential-dependent Brønsted – Evans – Polanyi (BEP) relation [79] between the intermediate with highest free energy and the transition state with highest free energy, which was validated in reference [55] by a comparison of DFT calculations and experimental data on single-crystalline model electrodes. It has been shown in previous studies that Eq. (32) can be used to describe experimental activity trends not only in a qualitative, but even in a quantitative fashion [75,80]. For further details, we refer to the literature [75].

Based on the partial current densities, $j_k(U)$, the total current density, $j(U)$, is obtained by summing all contributions of the individual mechanisms:

$$j(U) = \sum_k j_k(U) \tag{40}$$

The impact of a single span (for each reaction mechanism k) on the catalytic rate is called the potential-dependent degree of span control ($DSC_k(U)$ for mechanism k) and is expressed as:

$$DSC_k(U) = \frac{j_k(U)}{j(U)} \tag{41}$$

Fig. 4 illustrates this procedure by indicating the descriptor $G_{max}(U)$ for each mechanistic pathway and the corresponding $DSC_k(U)$ values in panels a) and b), respectively. Note that the relation of Eq. (35) must be fulfilled:

$$\sum_k DSC_k(U) = 1 \tag{42}$$

Fig. 4**a** highlights the potential-dependent changes in the activity descriptor $G_{max}(U)$ for the OER pathways considered. Different features are observed for the various mechanistic descriptions, which are discussed below. In case of the oxide mechanism, it is evident that the slope of the $G_{max}(U)$ *vs.* U plot remains unchanged in the entire potential range. This finding is related to a single elementary step that determines the descriptor $G_{max}(U)$ (*cf.* **Fig. S7** in section S6 of the SI). In contrast, other mechanisms, including the bifunctional-Walden description (*cf.* **Fig. S9** in section S6 of the SI), reveal a change in the slope of the $G_{max}(U)$ *vs.* U plot: in this case, the number of electrochemical steps governing $G_{max}(U)$ is reduced from two to one with increasing overpotential. On the other hand, it is also possible that the $G_{max}(U)$ *vs.* U relation becomes potential independent, such as encountered with the binuclear mechanism (*cf.* **Fig. S6** in section S6 of the SI). This finding is traced to a single chemical step that determines the descriptor $G_{max}(U)$, and thus the free-energy span is insensitive to an increase in the applied electrode potential. While chemical steps do not contribute to the

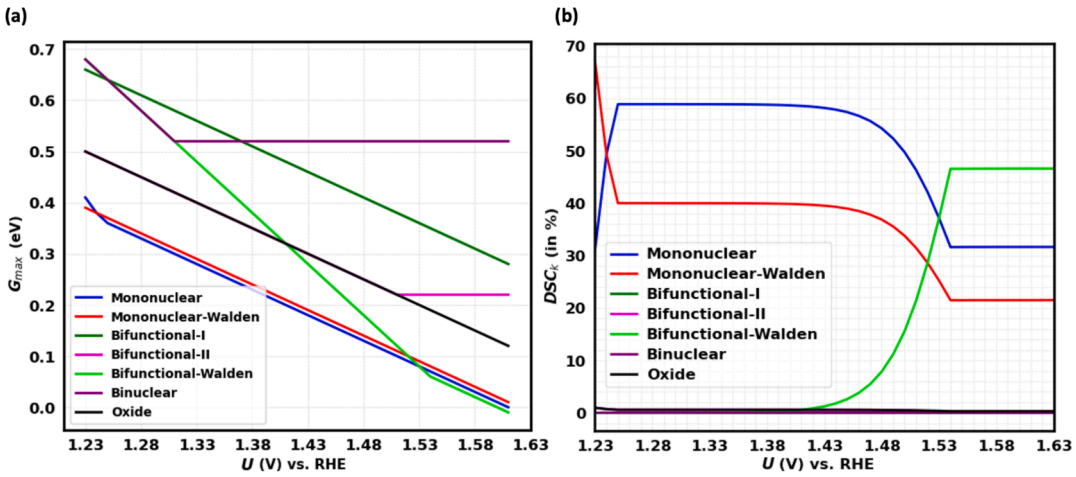

Fig. 4. a) Potential-dependent $G_{max}(U)$ values for seven mechanistic descriptions in the oxygen evolution reaction (OER) on Co_3O_4(001)-4*OH; **b)** Potential-dependent degree of span control (DSC_k) for the OER on Co_3O_4(001)-4*OH.

potential dependence of the free-energy span in the $G_{max}(U)$ *vs.* U relationship due to the application of the CHE approach, the number of electrochemical steps contributing to $G_{max}(U)$ varies between the different OER pathways, thus explaining the different potential dependencies in Fig. 4**a**.

Fig. 4**b** reveals that the mononuclear-Walden mechanism contributes almost 70 % to the current density at electrode potentials close to the OER equilibrium potential. With increasing electrode potential up to 1.30 V *vs.* RHE, the mononuclear description has the largest influence on the evolution of gaseous O_2 with a contribution of about 60 %, while the contribution of the mononuclear-Walden pathway steadily decreases. We relate these potential-dependent change in the $DSC_k(U)$ values to a different number of steps involved in the largest free-energy span governing the descriptor $G_{max}(U)$: for the mononuclear mechanism, a steeper decrease of $G_{max}(U)$ compared to the mononuclear-Walden description is observed in the range of 1.23 V < U *vs.* RHE < 1.28 V (*cf.* Fig. 4**a**) because the limiting span consists of two or one steps for the mononuclear and mononuclear-Walden pathway, respectively. Therefore, the $DSC_k(U)$ value of the mononuclear and mononuclear-Walden mechanisms increases or decreases, respectively, reminiscent of two different Tafel slopes for these mechanisms in this potential window (*cf.* **Figs. S3-S9** in section S6 of the SI).

For larger applied electrode potentials, the contribution of the bifunctional-Walden pathway to the current density becomes apparent, as the span of the descriptor $G_{max}(U)$ is reduced most efficiently (*cf.* Fig. 4**a**). The influence of the bifunctional-Walden mechanism increases to almost 50 % at an applied electrode potential of U = 1.55 *vs.* RHE, thus exceeding the impact of the mononuclear and mononuclear-Walden descriptions (*cf.* Fig. 4**b**). In summary, three different mechanisms – mononuclear, mononuclear-Walden, and bifunctional-Walden – contribute to the OER rate, and one of these pathways corresponds to the preferred description in a unique potential window. Therefore, the simplification of a single mechanism governing the kinetics of the OER over Co_3O_4(001)-4*OH is not met due to the significant contribution of all three pathways in terms of their $DSC_k(U)$ values.

We note that the bifunctional I, bifunctional II, binuclear, and oxide mechanisms do not contribute to the reaction rate of the OER over Co_3O_4(001)-4*OH. This is related to their $G_{max}(U)$ values (*cf.* Fig. 4**a**), which are more than 0.10 eV higher than those of the energetically favored mechanisms. Such a free-energy difference results in a negligible contribution to the reaction rate in terms of the $DSC_k(U)$ value due to the exponential relation between current density and $G_{max}(U)$ (*cf.* Eq. (39)). Therefore, a difference in $G_{max}(U)$ by 0.10 eV can be defined as a threshold for the identification of limiting mechanisms or limiting steps.

3.4. Potential-dependent contribution of the elementary reaction steps to the reaction rate, quantified by the degree of span control

While Fig. 4**b** underscores the impact of each reaction mechanism on the current density of the OER, it would be desirable to resolve the contribution of the elementary reaction steps or spans within the three favored pathways. Therefore, we analyze all possible free-energy spans, $S_{j,k}$, (*cf.* **Table S2** in section S5 of the SI) for the mononuclear, mononuclear-Walden, and bifunctional-Walden mechanisms by summing up their respective contribution for each mechanism individually in Eq. (36):

$$f_k(U) = \sum_j \mathrm{Exp}\left(\frac{+S_{j,k}(U)}{k_B \bullet T}\right) \tag{43}$$

In Eq. (36), $f_k(U)$ corresponds to the sum of all free-energy spans j for a mechanism k. This expression can be used to determine the relative contribution of a single span j for a given mechanism k:

$$DSC_{j,k}(U) = \frac{\exp\left(\frac{+S_{j,k}(U)}{k_B \bullet T}\right)}{f_k(U)} \bullet DSC_k(U) \tag{44}$$

Note that the relation of Eq. (38) needs to be fulfilled:

$$\sum_j DSC_{j,k}(U) = DSC_k(U) \tag{45}$$

We emphasize that the above procedure can be seen as a sensitivity analysis of the potential-dependent degree of span control ($DSC_k(U)$ for mechanism k), which is somewhat similar to Campbell's degree of rate control [10–13]. Following these lines, we determine $DSC_{j,k}(U)$ values, which indicate the potential-dependent degree of span control by relating them to the elementary steps within each reaction mechanism. For the OER over Co_3O_4(001)-4*OH (*cf.* Fig. 5), different elementary reaction steps contribute to the reaction rate to a different extent. While for the mononuclear and mononuclear-Walden descriptions the formation of surface oxygen, *OH →*O + (H^+ + e^-), corresponds to the limiting step in the entire potential window, the bifunctional-Walden pathway is mainly governed by the simultaneous desorption of O_2 and adsorption of H_2O for electrode potentials exceeding 1.50 V *vs.* RHE. Considering that certain steps are identical in the different pathways, such as the formation of surface oxygen in the mononuclear and mononuclear-Walden mechanisms, we summarize the relative contribution of these steps to derive $DSC_j(U)$ values that indicate the degree of span control for a span consisting of a single or several elementary steps j within all possible reaction mechanisms:

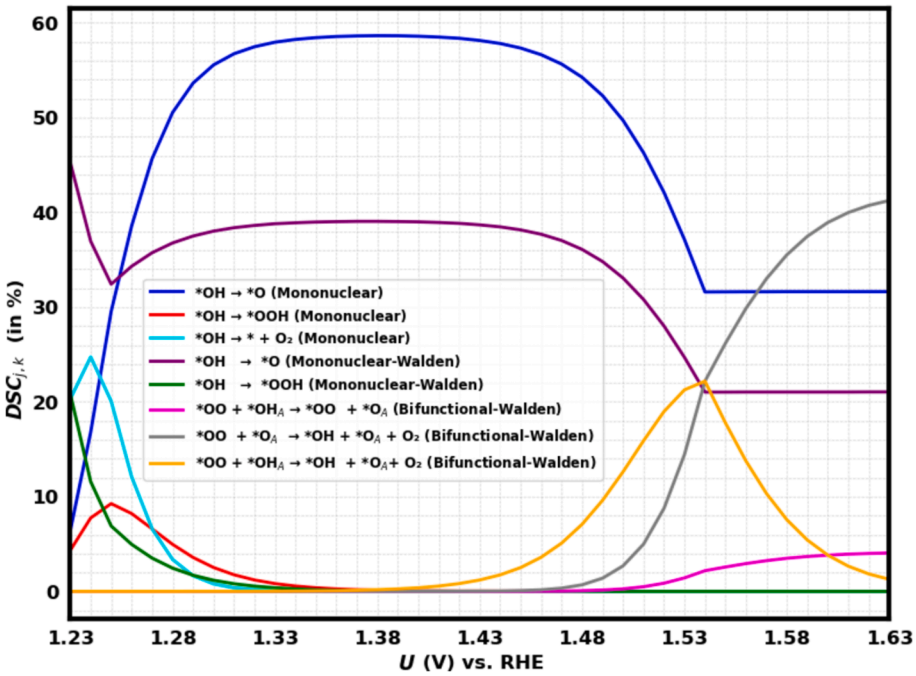

Fig. 5. Potential-dependent degree of span control ($DSC_{j,k}$) for the elementary steps of the mononuclear, mononuclear-Walden, and bifunctional-Walden mechanisms for the OER on Co_3O_4(001)-4*OH. Only spans with a relative contribution of at least 5 % in a certain potential window are indicated.

$$DSC_j(U) = \sum_k DSC_{j,k}(U) \tag{46}$$

Note that the relation of Eq. (40) needs to be fulfilled:

$$\sum_j DSC_j(U) = 1 \tag{47}$$

Fig. 6 depicts the $DSC_j(U)$ values of the elementary steps for the OER over Co_3O_4(001)-4*OH. Three different regions can be observed in dependence of the applied electrode potential.

a) 1.23 V < *U vs.* RHE < 1.30 V: different free-energy spans contribute to the reaction rate to a different extent. Besides the formation of surface oxygen, *OH →*O + ($H^+ + e^-$), the stabilization of the *OOH intermediate or the formation of gaseous O_2 govern the OER kinetics.
b) 1.30 V < *U vs.* RHE < 1.50 V: despite the presence of different reaction mechanisms in this potential range (*cf.* Fig. 4**b**), the OER kinetics is largely governed by the formation of surface oxygen, with a degree of span control close to 100 %.

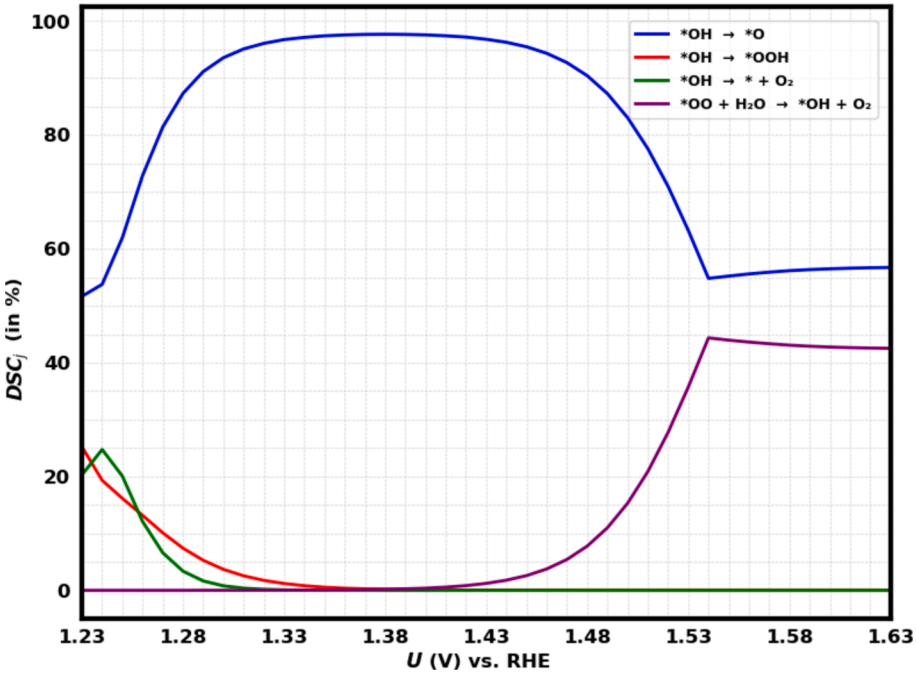

Fig. 6. Potential-dependent degree of span control (DSC_j) for the elementary steps of the OER on Co_3O_4(001)-4*OH. Only spans with a relative contribution of at least 5 % in a certain potential window are indicated.

c) *U vs.* RHE > 1.50 V: two elementary steps limit the OER rate to a similar extent, namely the formation of surface oxygen as well as the desorption of the product O_2 by means of a Walden-like step.

3.5. Subtleties of the degree of span control

Finally, we discuss the limitations of our approach to gain insights into the contribution of different mechanistic pathways and elementary steps to the OER rate. First, it needs to be emphasized that the consideration of transition states in the free-energy diagrams (*cf.* Fig. 3) can change the observed trends in terms of relevant mechanistic descriptions and limiting reaction steps to a certain extent. This fact is related to the assumed potential-dependent BEP relation (*cf.* Eq. (39)), which, however, has proven to be a good approximation for the discussion of the kinetics of electrocatalytic systems [55]. If the calculation of transition states based on DFT calculations is also computationally feasible for a variety of different mechanistic pathways, it is possible to directly apply Campbell's generalized degree of rate control to analyze the effect of mechanistic descriptions and elementary steps on the current density, as reported in previous contributions [69,70].

While theoretical works focusing on the calculation of transition states in an electrochemical environment are emerging in the literature [18,33,48,49,52,81,82], we emphasize that almost all of these works rely on the assessment of selected transition states in the catalytic cycle. Considering selected transition states, as opposed to calculating all transition states [83,84], is subject to bias because one assumes *a priori* which elementary steps limit the reaction rate. We do not think that such a procedure is justified because elementary steps limiting the reaction rate (to a certain extent) can be easily overlooked if their transition states are ignored in the analysis. To overcome this caveat, we purport that either a contemplation of the thermodynamic picture (focusing on the free energies of reaction intermediates only) or the consideration of all transition states in the catalytic cycle is needed for an unbiased assessment of reaction mechanisms and limiting reaction steps. While the latter is achieved by Campbell's degree of rate control, [10–13] the present contribution offers the exciting opportunity to discuss limiting steps and reaction mechanisms by sensitivity analyses using the degree of span control as a pure thermodynamic measure. As such, we do not claim that our presented approach of the degree of span control provides quantitative insight into operational mechanisms and limiting steps; rather we believe that our framework can be used to screen mechanistic pathways in a qualitative fashion to identify reaction mechanisms and steps where an in-depth investigation of the kinetic picture appears important.

3.6. Comparison with experimental data

Regarding the theoretical description of the OER on cobalt oxides, we are aware that it has been reported that Co_3O_4 undergoes reconstruction into CoOOH under the harsh anodic reaction conditions [85–88]. This phase transition depends on the crystallographic facet and has been observed for applied electrode potentials exceeding 1.62 V *vs.* RHE [62]. Therefore, we cannot guarantee that our theoretical model describes the experimentally active phase at large anodic overpotentials. For this reason, we limited our mechanistic analysis to an OER overpotential of 400 mV, which corresponds to 1.63 V *vs.* RHE. In addition, we also note that in this overpotential range, the Co_3O_4(001)-4*OH surface transforms to a mixed *OH/*O-covered surface (*cf.* Fig. 2). The mixed *OH/*O-covered surface could potentially serve as a precursor for the reconstruction of Co_3O_4 into CoOOH, in agreement with experimental studies [78,89]. Hence, for applied electrode potentials exceeding 1.50 V *vs.* RHE, the mechanistic picture of the OER on Co_3O_4(001) can be impacted by electrochemical processes beyond the seven considered reaction mechanisms in this work. Yet, the investigation of degradation or reconstruction processes on the Co_3O_4(001) surface is beyond the scope of the present contribution.

While previous theoretical studies reported a single elementary step as the kinetic bottleneck in the OER over cobalt oxides, [26–28,62] the present work highlights that several reaction mechanisms and elementary steps contribute to the OER rate as a function of applied electrode potential. Tschulik and coworkers reported by experiments on the single particle level that the (001) facet of Co_3O_4 outperforms other crystal facets in terms of OER activity [62]. Our detailed mechanistic study can explain this finding based on the assessment of the degree of span control, since the occurrence of multiple mechanisms during OER catalysis has been attributed to catalysts located at the volcano top [90].

Given that the introduced framework of the degree of span control relies on the thermodynamic part of the free-energy landscape, the presented approach can be easily transferred to other electrode materials with application in the OER or to electrocatalytic processes beyond electrochemical water splitting. We advocate coupling the degree of span control with artificial intelligence, including machine learning, to systematically analyze reaction networks, as this can help in identifying next-generation catalytic materials to overcome the current limitations resulting from the restriction to a single elementary step as a kinetic bottleneck.

4. Conclusions

Cobalt oxide is one of the most active and stable electrocatalysts for the anodic formation of gaseous oxygen by the oxygen evolution reaction (OER) under alkaline conditions. While previous theoretical studies identified limiting reaction steps according to the concept of the potential-determining step for a single mechanistic pathway, the present manuscript demonstrates that assuming a single reaction mechanism and discussing the kinetics with reference to a single limiting step is an oversimplification. We exemplify our viewpoint by modelling the OER over a single-crystalline Co_3O_4(001) electrode. After resolving the surface structure of this electrocatalyst under anodic reaction conditions (*cf.* Fig. 2), we consider seven different mechanistic pathways (*cf.* Fig. 1) while analyzing the elementary reaction steps by constructing free-energy diagrams (*cf.* Fig. 3).

To monitor the influence of the different reaction mechanisms on the OER over the active Co_3O_4(001)-4*OH configuration (*cf.* inset of Fig. 2), we introduce the concept of the potential-dependent degree of span control. These frameworks allow us to identify to which extent a certain mechanisms contributes to the OER rate. In case of the OER on Co_3O_4(001)-4*OH (*cf.* Fig. 4**b**), we observe that three different mechanistic descriptions – mononuclear, mononuclear-Walden, and bifunctional-Walden – efficiently catalyze the conversion of water to gaseous O_2. While each mechanism is somewhat favored in a particular potential window, the situation of a single pathway determining OER kinetics does not exist.

The potential-dependent degree of span control can also be exerted to determine the influence of the elementary reaction steps on the OER rate (*cf.* Fig. 6). While the formation of surface oxygen, *OH →*O + (H^+ + e^-), is identified as a key step for overpotentials as large as 400 mV, several other steps such as the stabilization of the *OOH intermediate or formation of the product O_2 are considered relevant for small or large OER overpotentials, respectively.

Given that the potential-dependent degree of span control enhances our mechanistic understanding of catalytic processes at electrified solid/liquid interfaces while being based on the thermodynamic picture of the free-energy landscape, this concept can be efficiently exploited for the screening of mechanistic pathways and limiting steps of catalysts for energy conversion processes. This knowledge can ultimately be used to derive refined activity and mechanistic trends of materials in a homologous series by moving beyond the conventional assumption of a single limiting reaction step in the analysis. Combining the potential-dependent degree of span control with artificial intelligence techniques can be helpful to guide the design of next-generation electrocatalysts through in-depth analyses of reaction networks.

CRediT authorship contribution statement

Kapil Dhaka: Data curation, Formal analysis, Investigation, Software, Validation, Visualization, Writing – original draft, Writing – review & editing. **Kai S. Exner:** Conceptualization, Funding acquisition, Methodology, Project administration, Resources, Supervision, Writing – original draft, Writing – review & editing.

Declaration of competing interest

The authors declare no competing interests.

Acknowledgments

KD and KSE acknowledge funding from the CRC/ TRR247: "Heterogeneous Oxidation Catalysis in the Liquid Phase" (Project number 388390466-TRR 247). KSE further thanks the RESOLV Cluster of Excellence, funded by the Deutsche Forschungsgemeinschaft under Germany's Excellence Strategy – EXC 2033 – 390677874 – RESOLV, for financial support. We thank Dr. Ebrahim Tayyebi (University of Duisburg-Essen) for fruitful discussions during preparation of this manuscript.

Appendix A. Supplementary data

Supplementary data to this article can be found online at https://doi.org/10.1016/j.jcat.2025.115970.

Data availability

All data required for the presented analysis is provided in the supplemental of this article.

References

[1] M. Chatenet, B.G. Pollet, D.R. Dekel, F. Dionigi, J. Deseure, P. Millet, R.D. Braatz, M.Z. Bazant, M. Eikerling, I. Staffell, P. Balcombe, Y. Shao-Horn, H. Schäfer, Water electrolysis: from textbook knowledge to the latest scientific strategies and industrial developments, Chem Soc Rev 51 (2022) 4583–4762, https://doi.org/10.1039/D0CS01079K.

[2] P.C.K. Vesborg, T.F. Jaramillo, Addressing the terawatt challenge: scalability in the supply of chemical elements for renewable energy, RSC Adv 2 (2012) 7933, https://doi.org/10.1039/c2ra20839c.

[3] C.C.L. McCrory, S. Jung, J.C. Peters, T.F. Jaramillo, Benchmarking heterogeneous electrocatalysts for the oxygen evolution reaction, J Am Chem Soc 135 (2013) 16977–16987, https://doi.org/10.1021/ja407115p.

[4] Y. Wang, M. Wang, Y. Yang, D. Kong, C. Meng, D. Zhang, H. Hu, M. Wu, Potential technology for seawater electrolysis: anion-exchange membrane water electrolysis, Chem Catal. 3 (2023) 100643, https://doi.org/10.1016/j.checat.2023.100643.

[5] T.O. Schmidt, A. Wark, R.W. Haid, R.M. Kluge, S. Suzuki, K. Kamiya, A. S. Bandarenka, J. Maruyama, E. Skúlason, Elucidating the active sites and synergies in water splitting on manganese oxide nanosheets on graphite support, Adv Energy Mater 13 (2023), https://doi.org/10.1002/aenm.202302039.

[6] M.J. Craig, G. Coulter, E. Dolan, J. Soriano-López, E. Mates-Torres, W. Schmitt, M. García-Melchor, Universal scaling relations for the rational design of molecular water oxidation catalysts with near-zero overpotential, Nat Commun 10 (2019) 4993, https://doi.org/10.1038/s41467-019-12994-w.

[7] H. Zhang, M. García-Melchor, Interrogating the oxygen evolution reaction mechanism at the atomic scale, Chem Catalysis 2 (2022) 1835–1837, https://doi.org/10.1016/j.checat.2022.07.012.

[8] I. Rodríguez-García, J.L. Gómez de la Fuente, D. Galyamin, Á. Tolosana-Moranchel, P. Kayser, M.A. Salam, J.A. Alonso, F. Calle-Vallejo, S. Rojas, M. Retuerto, Dy_2NiRuO_6 perovskite with high activity and durability for the oxygen evolution reaction in acidic electrolyte, J Mater Chem A Mater 12 (2024) 16854–16862, https://doi.org/10.1039/D3TA06788B.

[9] J.K. Nørskov, T. Bligaard, J. Rossmeisl, C.H. Christensen, Towards the computational design of solid catalysts, Nat Chem 1 (2009) 37–46, https://doi.org/10.1038/nchem.121.

[10] C.T. Campbell, Future directions and industrial perspectives micro- and macro-kinetics: their relationship in heterogeneous catalysis, Top Catal 1 (1994) 353–366, https://doi.org/10.1007/BF01492288.

[11] C.T. Campbell, The degree of rate control: a powerful tool for catalysis research, ACS Catal 7 (2017) 2770–2779, https://doi.org/10.1021/acscatal.7b00115.

[12] C.T. Campbell, Z. Mao, Analysis and prediction of reaction kinetics using the degree of rate control, J Catal 404 (2021) 647–660, https://doi.org/10.1016/j.jcat.2021.10.002.

[13] C. Stegelmann, A. Andreasen, C.T. Campbell, Degree of rate control: how much the energies of intermediates and transition states control rates, J Am Chem Soc 131 (2009) 8077–8082, https://doi.org/10.1021/ja9000097.

[14] Z.W. Seh, J. Kibsgaard, C.F. Dickens, I. Chorkendorff, J.K. Nørskov, T.F. Jaramillo, Combining theory and experiment in electrocatalysis: insights into materials design, Science 1979 (2017) 355, https://doi.org/10.1126/science.aad4998.

[15] N. Govindarajan, G. Kastlunger, H.H. Heenen, K. Chan, Improving the intrinsic activity of electrocatalysts for sustainable energy conversion: where are we and where can we go? Chem Sci 13 (2022) 14–26, https://doi.org/10.1039/D1SC04775B.

[16] G. Kastlunger, P. Lindgren, A.A. Peterson, Controlled-potential simulation of elementary electrochemical reactions: proton discharge on metal surfaces, J. Phys. Chem. C 122 (2018) 12771–12781, https://doi.org/10.1021/acs.jpcc.8b02465.

[17] E. Tayyebi, Y. Abghoui, E. Skúlason, Elucidating the mechanism of electrochemical N_2 reduction at the Ru(0001) electrode, ACS Catal 9 (2019) 11137–11145, https://doi.org/10.1021/acscatal.9b03903.

[18] N. Abidi, S.N. Steinmann, How are transition states modeled in heterogeneous electrocatalysis? Curr Opin Electrochem 33 (2022) 100940 https://doi.org/10.1016/j.coelec.2022.100940.

[19] J.K. Nørskov, J. Rossmeisl, A. Logadottir, L. Lindqvist, J.R. Kitchin, T. Bligaard, H. Jónsson, Origin of the overpotential for oxygen reduction at a fuel-cell cathode, J Phys Chem B 108 (2004) 17886–17892, https://doi.org/10.1021/jp047349j.

[20] S. Singh, F. Bononi, O. Andreussi, N. Karmodak, Thermodynamic and kinetic modeling of electrocatalytic reactions using a first-principles approach, J Chem Phys 159 (2023), https://doi.org/10.1063/5.0165835.

[21] L.C. Seitz, C.F. Dickens, K. Nishio, Y. Hikita, J. Montoya, A. Doyle, C. Kirk, A. Vojvodic, H.Y. Hwang, J.K. Norskov, T.F. Jaramillo, A highly active and stable $IrO_x/SrIrO_3$ catalyst for the oxygen evolution reaction, Science 353 (2016) (1979) 1011–1014, https://doi.org/10.1126/science.aaf5050.

[22] M.T.M. Koper, Analysis of electrocatalytic reaction schemes: distinction between rate-determining and potential-determining steps, J. Solid State Electrochem. 17 (2013) 339–344, https://doi.org/10.1007/s10008-012-1918-x.

[23] M.T.M. Koper, Theory of multiple proton–electron transfer reactions and its implications for electrocatalysis, Chem Sci 4 (2013) 2710, https://doi.org/10.1039/c3sc50205h.

[24] K.S. Exner, Standard-state entropies and their impact on the potential-dependent apparent activation energy in electrocatalysis, Journal of Energy Chemistry 83 (2023) 247–254, https://doi.org/10.1016/j.jechem.2023.04.020.

[25] F.T. Haase, A. Bergmann, T.E. Jones, J. Timoshenko, A. Herzog, H.S. Jeon, C. Rettenmaier, B.R. Cuenya, Size effects and active state formation of cobalt oxide nanoparticles during the oxygen evolution reaction, Nat Energy 7 (2022) 765–773, https://doi.org/10.1038/s41560-022-01083-w.

[26] Y. Peng, H. Hajiyani, R. Pentcheva, Influence of fe and ni doping on the oer performance at the co3o4(001) surface: insights from DFT+u calculations, ACS Catal 11 (2021) 5601–5613, https://doi.org/10.1021/acscatal.1c00214.

[27] M. Bajdich, M. García-Mota, A. Vojvodic, J.K. Nørskov, A.T. Bell, Theoretical investigation of the activity of cobalt oxides for the electrochemical oxidation of water, J Am Chem Soc 135 (2013) 13521–13530, https://doi.org/10.1021/ja405997s.

[28] M. García-Mota, M. Bajdich, V. Viswanathan, A. Vojvodic, A.T. Bell, J.K. Nørskov, Importance of correlation in determining electrocatalytic oxygen evolution activity on cobalt oxides, J. Phys. Chem. C 116 (2012) 21077–21082, https://doi.org/10.1021/jp306303y.

[29] K. Bhattacharyya, A.A. Auer, oxygen evolution reaction electrocatalysis on cobalt (oxy)hydroxide: role of fe impurities, J. Phys. Chem. C 126 (2022) 18623–18635, https://doi.org/10.1021/acs.jpcc.2c06436.

[30] J. Rossmeisl, A. Logadottir, J.K. Nørskov, Electrolysis of water on (oxidized) metal surfaces, Chem Phys 319 (2005) 178–184, https://doi.org/10.1016/j.chemphys.2005.05.038.

[31] K.S. Exner, On the mechanistic complexity of oxygen evolution: potential-dependent switching of the mechanism at the volcano apex, Mater Horiz 10 (2023) 2086–2095, https://doi.org/10.1039/D3MH00047H.

[32] H.M.A. Amin, H. Baltruschat, How many surface atoms in Co_3O_4 take part in oxygen evolution? Isotope labeling together with differential electrochemical mass spectrometry, Physical Chemistry Chemical Physics 19 (2017) 25527–25536, https://doi.org/10.1039/C7CP03914J.

[33] Z. Wang, W.A. Goddard, H. Xiao, Potential-dependent transition of reaction mechanisms for oxygen evolution on layered double hydroxides, Nat Commun 14 (2023) 4228, https://doi.org/10.1038/s41467-023-40011-8.

[34] A. Zagalskaya, I. Evazzade, V. Alexandrov, *Ab initio* thermodynamics and kinetics of the lattice oxygen evolution reaction in iridium oxides, ACS Energy Lett 6 (2021) 1124–1133, https://doi.org/10.1021/acsenergylett.1c00234.

[35] A. Zagalskaya, V. Alexandrov, Role of defects in the interplay between adsorbate evolving and lattice oxygen mechanisms of the oxygen evolution reaction in RuO_2 and IrO_2, ACS Catal 10 (2020) 3650–3657, https://doi.org/10.1021/acscatal.9b05544.

[36] J. Zhang, G. Chen, D. Sun, Y. Tang, W. Xing, H. Sun, X. Feng, Regulating Co–O covalency to manipulate mechanistic transformation for enhancing activity/durability in acidic water oxidation, Chem Sci (2024), https://doi.org/10.1039/D4SC05547K.

[37] F. Hess, H. Over, Coordination inversion of the tetrahedrally coordinated Ru_{4f} surface complex on RuO_2 (100) and its decisive role in the anodic corrosion

process, ACS Catal 13 (2023) 3433–3443, https://doi.org/10.1021/acscatal.2c06260.
[38] K.S. Exner, Importance of the walden inversion for the activity volcano plot of oxygen evolution, Adv. Sci. 10 (2023), https://doi.org/10.1002/advs.202305505.
[39] S. Yu, Z. Levell, Z. Jiang, X. Zhao, Y. Liu, What is the rate-limiting step of oxygen reduction reaction on Fe–N–C catalysts? J Am Chem Soc 145 (2023) 25352–25356, https://doi.org/10.1021/jacs.3c09193.
[40] G. Kresse, J. Hafner, Ab initio molecular dynamics for open-shell transition metals, PhysRevB 48 (1993) 13115–13118, https://doi.org/10.1103/PhysRevB.48.13115.
[41] G. Kresse, J. Furthmüller, Efficiency of ab-initio total energy calculations for metals and semiconductors using a plane-wave basis set, Comput Mater Sci 6 (1996) 15–50, https://doi.org/10.1016/0927-0256(96)00008-0.
[42] G. Kresse, J. Furthmüller, Efficient iterative schemes for ab initio total-energy calculations using a plane-wave basis set, PhysRevB 54 (1996) 11169–11186, https://doi.org/10.1103/PhysRevB.54.11169.
[43] K. Mathew, R. Sundararaman, K. Letchworth-Weaver, T.A. Arias, R.G. Hennig, Implicit solvation model for density-functional study of nanocrystal surfaces and reaction pathways, J Chem Phys 140 (2014), https://doi.org/10.1063/1.4865107.
[44] M. Sokolov, K.S. Exner, Is the *O vs. *OH scaling relation intercept more relevant than the *OOH vs. *OH intercept to capture trends in the oxygen evolution reaction? Chem Catalysis 4 (2024) 101039 https://doi.org/10.1016/j.checat.2024.101039.
[45] J. Rossmeisl, Z.W. Qu, H. Zhu, G.J. Kroes, J.K. Nørskov, Electrolysis of water on oxide surfaces, J. Electroanal. Chem. 607 (2007) 83–89, https://doi.org/10.1016/j.jelechem.2006.11.008.
[46] N.B. Halck, V. Petrykin, P. Krtil, J. Rossmeisl, Beyond the volcano limitations in electrocatalysis – oxygen evolution reaction, Phys. Chem. Chem. Phys. 16 (2014) 13682–13688, https://doi.org/10.1039/C4CP00571F.
[47] H.N. Nong, L.J. Falling, A. Bergmann, M. Klingenhof, H.P. Tran, C. Spöri, R. Mom, J. Timoshenko, G. Zichittella, A. Knop-Gericke, S. Piccinin, J. Pérez-Ramírez, B. R. Cuenya, R. Schlögl, P. Strasser, D. Teschner, T.E. Jones, Key role of chemistry versus bias in electrocatalytic oxygen evolution, Nature 587 (2020) 408–413, https://doi.org/10.1038/s41586-020-2908-2.
[48] Y.-H. Fang, Z.-P. Liu, Mechanism and Tafel lines of electro-oxidation of water to oxygen on RuO_2 (110), J Am Chem Soc 132 (2010) 18214–18222, https://doi.org/10.1021/ja1069272.
[49] Y. Ping, R.J. Nielsen, W.A. Goddard, The reaction mechanism with free energy barriers at constant potentials for the oxygen evolution reaction at the IrO_2 (110) surface, J Am Chem Soc 139 (2017) 149–155, https://doi.org/10.1021/jacs.6b07557.
[50] M. Busch, Water oxidation: from mechanisms to limitations, Curr Opin Electrochem 9 (2018) 278–284, https://doi.org/10.1016/j.coelec.2018.06.007.
[51] M. Busch, E. Ahlberg, I. Panas, Electrocatalytic oxygen evolution from water on a Mn(iii–v) dimer model catalyst—A DFT perspective, PCCP 13 (2011) 15069, https://doi.org/10.1039/c0cp02132f.
[52] T. Binninger, M.-L. Doublet, The Ir–OOOO–Ir transition state and the mechanism of the oxygen evolution reaction on IrO_2 (110), Energy, Environ Sci 15 (2022) 2519–2528, https://doi.org/10.1039/D2EE00158F.
[53] K.S. Exner, Implications of the M-OO●●OO-M recombination mechanism on materials screening and the oxygen evolution reaction, Journal of Physics: Energy 5 (2023) 014008, https://doi.org/10.1088/2515-7655/aca82a.
[54] S. Razzaq, S. Faridi, S. Kenmoe, M. Usama, D. Singh, L. Meng, F. Vines, F. Illas, K. S. Exner, MXenes spontaneously form active and selective single-atom centers under anodic polarization conditions, J. Am. Chem. Soc. 147 (2025) 161–168.
[55] K.S. Exner, A universal descriptor for the screening of electrode materials for multiple-electron processes: beyond the thermodynamic overpotential, ACS Catal 10 (2020) 12607–12617, https://doi.org/10.1021/acscatal.0c03865.
[56] S. Kozuch, S. Shaik, How to conceptualize catalytic cycles? The energetic span model, Acc Chem Res 44 (2011) 101–110, https://doi.org/10.1021/ar1000956.
[57] M. Usama, S. Razzaq, K.S. Exner, Design criteria for active and selective catalysts in the nitrogen oxidation reaction, ACS Phys. Chem. Au (2024), https://doi.org/10.1021/acsphyschemau.4c00058.
[58] S. Razzaq, K.S. Exner, Materials screening by the descriptor Gmax(η): the free-energy span model in electrocatalysis, ACS Catal 13 (2023) 1740–1758, https://doi.org/10.1021/acscatal.2c03997.
[59] H.A. Hansen, J. Rossmeisl, J.K. Nørskov, Surface Pourbaix diagrams and oxygen reduction activity of Pt, Ag and Ni(111) surfaces studied by DFT, PCCP 10 (2008) 3722, https://doi.org/10.1039/b803956a.
[60] A. Groß, Grand-canonical approaches to understand structures and processes at electrochemical interfaces from an atomistic perspective, Curr Opin Electrochem 27 (2021) 100684, https://doi.org/10.1016/j.coelec.2020.100684.
[61] A.M. Verma, L. Laverdure, M.M. Melander, K. Honkala, Mechanistic origins of the pH dependency in Au-catalyzed glycerol electro-oxidation: insight from first-principles calculations, ACS Catal 12 (2022) 662–675, https://doi.org/10.1021/acscatal.1c03788.
[62] Z. Liu, H.M.A. Amin, Y. Peng, M. Corva, R. Pentcheva, K. Tschulik, Facet-dependent intrinsic activity of single co3o4 nanoparticles for oxygen evolution reaction, Adv Funct Mater 33 (2023), https://doi.org/10.1002/adfm.202210945.
[63] P. Clabaut, B. Schweitzer, A.W. Götz, C. Michel, S.N. Steinmann, Solvation free energies and adsorption energies at the metal/water interface from hybrid quantum-mechanical/molecular mechanics simulations, J Chem Theory Comput 16 (2020) 6539–6549, https://doi.org/10.1021/acs.jctc.0c00632.
[64] Z. Liu, H.M.A. Amin, Y. Peng, M. Corva, R. Pentcheva, K. Tschulik, Facet-dependent intrinsic activity of single Co_3O_4 nanoparticles for oxygen evolution reaction, Adv Funct Mater 33 (2023), https://doi.org/10.1002/adfm.202210945.
[65] J. Huang, X. Zhu, M. Eikerling, The rate-determining term of electrocatalytic reactions with first-order kinetics, Electrochim Acta 393 (2021) 139019, https://doi.org/10.1016/j.electacta.2021.139019.
[66] F. Calle-Vallejo, M.T.M. Koper, First-principles computational electrochemistry: achievements and challenges, Electrochim Acta 84 (2012) 3–11, https://doi.org/10.1016/j.electacta.2012.04.062.
[67] O. van der Heijden, S. Park, R.E. Vos, J.J.J. Eggebeen, M.T.M. Koper, Tafel slope plot as a tool to analyze electrocatalytic reactions, ACS Energy Lett 9 (2024) 1871–1879, https://doi.org/10.1021/acsenergylett.4c00266.
[68] T. Shinagawa, A.T. Garcia-Esparza, K. Takanabe, Insight on Tafel slopes from a microkinetic analysis of aqueous electrocatalysis for energy conversion, Sci Rep 5 (2015) 13801, https://doi.org/10.1038/srep13801.
[69] A. Baz, S.T. Dix, A. Holewinski, S. Linic, Microkinetic modeling in electrocatalysis: applications, limitations, and recommendations for reliable mechanistic insights, J Catal 404 (2021) 864–872, https://doi.org/10.1016/j.jcat.2021.08.043.
[70] A. Baz, A. Holewinski, Predicting macro-kinetic observables in electrocatalysis using the generalized degree of rate control, J Catal 397 (2021) 233–244, https://doi.org/10.1016/j.jcat.2021.03.014.
[71] K. Chan, J.K. Nørskov, Electrochemical barriers made simple, J Phys Chem Lett 6 (2015) 2663–2668, https://doi.org/10.1021/acs.jpclett.5b01043.
[72] H. Jing, P. Zhu, X. Zheng, Z. Zhang, D. Wang, Y. Li, Theory-oriented screening and discovery of advanced energy transformation materials in electrocatalysis, Adv. Powder Mater. 1 (2022) 100013, https://doi.org/10.1016/j.apmate.2021.10.004.
[73] F.A. Rasmussen, K.S. Thygesen, Computational 2D materials database: electronic structure of transition-metal dichalcogenides and oxides, J. Phys. Chem. C 119 (2015) 13169–13183, https://doi.org/10.1021/acs.jpcc.5b02950.
[74] J. Greeley, T.F. Jaramillo, J. Bonde, I. Chorkendorff, J.K. Nørskov, Computational high-throughput screening of electrocatalytic materials for hydrogen evolution, Nat Mater 5 (2006) 909–913, https://doi.org/10.1038/nmat1752.
[75] K.S. Exner, I. Sohrabnejad-Eskan, H. Over, A universal approach to determine the free energy diagram of an electrocatalytic reaction, ACS Catal 8 (2018) 1864–1879, https://doi.org/10.1021/acscatal.7b03142.
[76] K.S. Exner, Why the microkinetic modeling of experimental tafel plots requires knowledge of the reaction intermediate's binding energy, Electrochem. Sci. Adv. 2 (2022), https://doi.org/10.1002/elsa.202100037.
[77] P. Khadke, T. Tichter, T. Boettcher, F. Muench, W. Ensinger, C. Roth, A simple and effective method for the accurate extraction of kinetic parameters using differential Tafel plots, Sci Rep 11 (2021) 8974, https://doi.org/10.1038/s41598-021-87951-z.
[78] A. Holewinski, S. Linic, Elementary mechanisms in electrocatalysis: revisiting the ORR tafel slope, J Electrochem Soc 159 (2012) H864–H870, https://doi.org/10.1149/2.022211jes.
[79] R.A. van Santen, M. Neurock, S.G. Shetty, Reactivity theory of transition-metal surfaces: a brønsted−evans−polanyi linear activation energy−free-energy analysis, Chem Rev 110 (2010) 2005–2048, https://doi.org/10.1021/cr9001808.
[80] A. Ciotti, M. García-Melchor, The importance of surface coverages in the rational design of electrocatalysts, Curr Opin Electrochem 42 (2023) 101402, https://doi.org/10.1016/j.coelec.2023.101402.
[81] J. Long, D. Luan, X. Fu, H. Li, H. Jing, J. Xiao, Fundamental insights on the electrochemical nitrogen oxidation over metal oxides, ACS Catal 14 (2024) 4423–4431, https://doi.org/10.1021/acscatal.3c05307.
[82] H. Jing, J. Long, H. Li, X. Fu, J. Xiao, Computational insights on electrocatalytic synthesis of methylamine from nitrate and carbon dioxide, ACS Catal 13 (2023) 9925–9935, https://doi.org/10.1021/acscatal.3c01592.
[83] K.S. Exner, J. Anton, T. Jacob, H. Over, Full kinetics from first principles of the chlorine evolution reaction over a RuO_2 (110) model electrode, Angew. Chem. Int. Ed. 55 (2016) 7501–7504, https://doi.org/10.1002/anie.201511804.
[84] M. López, K.S. Exner, F. Viñes, F. Illas, Theoretical study of the mechanism of the hydrogen evolution reaction on the V2C MXene: thermodynamic and kinetic aspects, J Catal 421 (2023) 252–263, https://doi.org/10.1016/j.jcat.2023.03.027.
[85] H. Li, X. Weng, Y. Kang, H. Lei, Y. Li, C. Zhou, R. Huang, Y. Kong, T. Liu, W. Wei, Z. Gong, D. Ding, Z. Chen, Y. Cui, Observing the reconstruction of cobalt oxide model catalyst in electrocatalytic water oxidation, Appl Surf Sci 644 (2024) 158734, https://doi.org/10.1016/j.apsusc.2023.158734.
[86] J. Huang, H. Sheng, R.D. Ross, J. Han, X. Wang, B. Song, S. Jin, Modifying redox properties and local bonding of Co3O4 by CeO2 enhances oxygen evolution catalysis in acid, Nat Commun 12 (2021) 3036, https://doi.org/10.1038/s41467-021-23390-8.
[87] Z. Liu, M. Corva, H.M.A. Amin, N. Blanc, J. Linnemann, K. Tschulik, Single Co3O4 nanocubes electrocatalyzing the oxygen evolution reaction: nano-impact insights into intrinsic activity and support effects, Int J Mol Sci 22 (2021) 13137, https://doi.org/10.3390/ijms222313137.
[88] C. Luan, M. Corva, U. Hagemann, H. Wang, M. Heidelmann, K. Tschulik, T. Li, Atomic-Scale insights into morphological, structural, and compositional evolution of CoOOH during oxygen evolution reaction, ACS Catal 13 (2023) 1400–1411, https://doi.org/10.1021/acscatal.2c03903.
[89] L. Xu, Q. Jiang, Z. Xiao, X. Li, J. Huo, S. Wang, L. Dai, Plasma-Engraved Co_3O_4 nanosheets with oxygen vacancies and high surface area for the oxygen evolution reaction, Angew. Chem. Int. Ed. 55 (2016) 5277–5281, https://doi.org/10.1002/anie.201600687.
[90] K.S. Exner, Four generations of volcano plots for the oxygen evolution reaction: beyond proton-coupled electron transfer steps? Acc Chem Res 57 (2024) 1336–1345, https://doi.org/10.1021/acs.accounts.4c00048.